Journal of Materials Chemistry A

Chemical-enzymatic fractionation to unlock the potential of biomass-derived carbon materials for sodium ion batteries

Journal:	*Journal of Materials Chemistry A*
Manuscript ID	TA-ART-08-2019-009124.R1
Article Type:	Paper
Date Submitted by the Author:	28-Oct-2019
Complete List of Authors:	Feng, Yiming; Virginia Polytechnic Institute and State University, Department of Food Science and Technology Tao, Lei; Virginia Tech He, Yanhong; Virginia Tech Jin, Qing; Virginia Tech Zheng, Yunwu; Northeast Forestry University, Kuai, Chunguang; Virginia Polytechnic Institute and State University Li, Mengqiao ; George Washington University Hou, Qingping; Virginia Tech Zheng, Zhifeng; Xiamen University, Xiamen 361102, P.R. China, College of Energy Lin, Feng; Virginia Polytechnic Institute and State University, Chemistry Huang, Haibo; Virginia Tech, Department of Food Science and Technology

Chemical-enzymatic fractionation to unlock the potential of biomass-derived carbon materials for sodium ion batteries

Yiming Feng,[£1] Lei Tao,[£2,3] Yanhong He,[1] Qing Jin,[1] Chunguang Kuai,[3] Yunwu Zheng,[4] Mengqiao Li,[5] Qingping Hou,[3] Zhifeng Zheng,[2] Feng Lin,[3,*] Haibo Huang[1,*]

1. Department of Food Science and Technology, Virginia Tech, Blacksburg, Virginia 24061, United States.
2. College of Energy, Xiamen University, Xiamen, Fujian 361102, China.
3. Department of Chemistry, Virginia Tech, Blacksburg, Virginia 24061, United States.
4. College of Materials Engineering, Southwest Forestry University, Kunming 650224, China.
5. Department of Civil and Environmental Engineering, The George Washington University, Washington, DC 20052, United States

[£]The authors contributed equally to this work.

[*]Corresponding authors

F.L.: fenglin@vt.edu; H.H.: huang151@vt.edu

Abstract

Plant biomass, the most abundant and sustainable carbon source, offers a rich chemical space to design hard carbons for sodium ion batteries. However, the compositional complexity of biomass has for a long time compromised the predictability of the carbon structural and electrochemical properties. Using chemical-enzymatic fractionation technique, we successively remove non-lignocellulosic component, hemicellulose and cellulose to create a suite of precursors for carbonization, in order to understand the roles of each biomass component in battery performance. Brewer's spent grain, an agricultural waste, is used as a representative biomass platform. The resulting hard carbon, with non-lignocellulosic components removed prior to carbonization, exhibits a dramatically reduced surface area and an increased specific capacity. Simultaneously removing non-lignocellulosic components and hemicellulose results in more sp^2 carbon, expanded (002) interlayer spacing, and a remarkably improved specific capacity by four folds. Further removing cellulose, with only lignin remained, significantly reduces the sp^2 carbon and undermines the cycling stability of the derived carbon. Our finding reveals that the electrochemical

properties of the biomass-derived hard carbons in sodium ion batteries may be positively correlated with cellulose and lignin but negatively impacted by non-lignocellulosic components and hemicellulose. Guided by this knowledge, we further fractionated two additional biomass, i.e. grape pomace and walnut shells, for improving the carbon performance. After removing non-lignocellulosic component and hemicellulose, the resulting hard carbon delivers a reversible capacity of 296 mAh g^{-1} at 50 mA g^{-1} and retains 86.4% capacity after 200 cycles. Therefore, our results lay the foundation for unlocking the potential of biomass-derived carbon materials by precise fractionation of biomass components.

Introduction

Graphite has been commercialized as anodes in lithium ion batteries[1]; however, it has been proven not optimal for sodium ion batteries due to its inferior sodium ion storage capability[2–4]. Instead, biomass-derived hard carbons have demonstrated promising potential for sodium ion batteries. To date, numerous studies have been conducted to produce hard carbons from a broad range of biological sources, including animals[5,6], microorganisms[7,8] and plants[9]. Comparing to animal- and microorganism-based biomasses, plant-based biomass are considered as a more practical source because of their low cost, availability and abundancy[10,11]. Therefore, the majority of previous work focused on converting plant-based biomasses into functional carbon materials via carbonization [12], a thermochemical process to increase the carbon content by removing other elements[13]. However, even within the category of plant-based biomasses, depending on the chemical composition of different biomass precursors, processing routes and catalysts being used, the physicochemical and electrochemical properties of the derived carbon materials drastically vary. Previous studies reported that hard carbon materials derived from plant-based biomass deliver variable specific capacities and cycling performance in sodium ion batteries[14–18]. Such a remarkable difference could be a ramification of a series of factors, and it is widely accepted that the chemical composition of biomass is inevitably playing one of the decisive roles[19,20].

Plant-based biomasses are generally composed of lignocellulosic components, proteins, lipids, soluble extracts and other inorganic minerals[21], among which the lignocellulosic components (cellulose, hemicellulose and lignin) constitutes the majority of the total weight[22–24]. Although cellulose, hemicellulose and lignin are polymeric compounds, their chemical and physical properties vary distinctively. Cellulose is a homopolysacchrides consisting of anhydro-glucan

units linked by β-(1,4)-glycosidic bonds[25]. Depending on the biological origin and degree of polymerization, the molecular weight of cellulose could vary[26]. Hemicellulose and lignin are more complex, since their constituent monomers are heterogeneous. The monosaccharide units comprising hemicellulose include pentoses (xylose and arabinose) and hexoses (glucose, mannose, and galactose), as well as other saccharides[27]. Similarly, the physicochemical properties of lignin are depending on the fraction ratios of three monomer units: p-hydroxyphenyl (H), guaiacyl (G), and syringyl (S)[28].

During the carbonization process, cellulose, hemicellulose and lignin from the biomass are decomposed at different temperatures through their specific pathways and kinetics[29–31], along with complex interactions with other components (e.g. minerals) to form char structures[32,33]. Each lignocellulosic component follows a certain decomposition pathway to reach their chemical fates as affected by the thermochemical treatment conditions, such as holding temperature and heating rate[34–36]. Hemicellulose and cellulose behave distinctively in the thermochemical treatment, primarily due to the differences in their decomposition temperatures and pathways[37]. Hemicellulose tends to depolymerize and degrade at a relatively lower temperature (< 300 °C), while cellulose requires a higher temperature (~ 400 °C) due its more crystalline structure[29]. On the other hand, lignin presents a completely amorphous structure, with highly crosslinked polymeric monomer units, which results in a wide range of thermal degradation temperature and slow reaction kinetics[29]. Therefore, varying the ratios among these three lignocellulosic components would remarkably alter the reaction intermediates and kinetics, which further lead to the formation of carbon materials with substantially distinct features.

The compositional effects of biomasses on the energy storage performance of biomass-derived hard carbons have been attempted by a few pioneering studies via a direct comparison of different whole biomass precursors [20,38]. However, it is still unknown how does each specific component, especially the major component of cellulose, hemicellulose and lignin, affect the resulting carbon properties and the corresponding battery performance. Herein, we first-time report a chemical-enzymatic approach to manipulate the major composition in biomass, with the aim to incisively understand the roles of individual biomass components in determining the structural and electrochemical properties of hard carbons. The gained new knowledge will help advance the

rational selection and fractionation of the abundant and sustainable biomass for sodium ion batteries.

Materials and methods

Chemical-enzymatic fractionation

The raw biomass was grinded using a Hammer mill (MF 10 basic, IKA, Germany) and the powders smaller than 500 μm were collected. A composition analysis on the dried biomass samples were performed following the standard chemical method established by the National Renewable Energy Laboratory (NREL)[39]. The grounded samples were readily named as raw biomasses. Further fractionation of biomasses was achieved by a fiber analyzing system[40] (ANKOM 2000, ANKOM Technology, New York) through a bag-filtration process. Neutral detergent solution and acid detergent solution were used in the chemical-enzymatic fractionation processes to remove non-lignocellulosic components (proteins, minerals, starch, lipid) and hemicellulose to generate neutral detergent fiber (NDF) and acid detergent fiber (ADF), respectively. The neutral detergent solution (ANKOM FND20) contains sodium lauryl sulfate (3%, w/v), EDTA disodium (1.86%, w/v), triethylene glycol (1%, w/v), sodium borate (0.68%, w/v), sodium phosphate (0.46%, w/v). Sodium sulfite (20 g) and α-amylase (8 ml) (ANKOM FAA, activity = 17,400 Units/ml) were also used with the NDF detergent. The acid detergent solution (ANKOM FAD20CB) contains sulfuric acid (2.93%, w/v), and cetyltrimethylammonium bromide (2%, w/v). Both of the NDF and ADF fractionation processes are programmed procedures that involve high temperature treatment (105 °C), elevated pressure (15 – 20 psi) and extensive shaking for 60 min to ensure a complete reaction[41,42]. The NDF is a mixture of cellulose, hemicellulose and lignin, while the ADF is a mixture of cellulose of lignin. The ADF are further subjected to 72% (w/w) H_2SO_4 for 1 hour at 30 °C, followed by an acidic hydrolysis (3% H_2SO_4, 120 °C, 1 hour) to effectively remove crystal cellulose to derive Klason Lignin.

Carbonization

The fractions derived from each biomass are subjected to a carbonization process at 800 °C and 1050 °C in a tube furnace under constant nitrogen flow, and the temperature ramping rate is set at 5 °C/min. The derived carbons are named as Raw_C, NDF_C, ADF_C and Lignin_C, respectively.

Carbon characterization

The morphology of biomass-derived carbons was characterized using scanning electron microscope (FESEM, LEO 1550) and high-resolution transmission electron microscopy (HRTEM, JEOL JEM 2100). Structural proprieties of biomass-derived carbons from different fractions of biomass were characterized. The polymorphism of carbonized biomass was characterized by X-ray diffraction patterns (XRD, Shimadzu, Japan) using Cu-Kα radiation (wavelength λ= 1.5406 Å). The Bruker-Emmett-Teller (BET) method was utilized to calculate the specific surface area, by a fully automatic physical adsorption apparatus (ASAP 2020 Plus HD88, Micromeritics Co., Ltd.) at -196 °C after outgassed at 200 °C for 12 h under vacuum. The pore size distribution was obtained from the adsorption branches of the isotherms by the density functional theory (DFT) method. Raman Spectra were collected with a WITec alpha500R instrument using a 532 nm excitation source. Two peaks at around 1350 - 1370 cm^{-1} and 1580 - 1600 cm^{-1} were identified as "D" and "G" bands, which correspond to the defected carbon (D band) and the sp^2-bonded graphitic carbon structures (G band). The ratio between two peak areas (I_G/I_D) was calculated. X-ray photoelectron spectroscopy (XPS) measurements were conducted with a scanning photoelectron spectrometer microprobe (PHI Quantera SXM, ULVAC-PHI Inc., Japan), which was equipped with an Al anode as the monochromatized X-ray source to investigate the surface composition and the valence state. A high-resolution scan was performed for C 1s and O 1s.

Electrochemical tests in half-cells

The composite electrodes were fabricated by mixing biomass-derived carbons, carbon black and polytetrafluoroethylene (PVDF) binder in a mass ratio of 8:1:1 on a copper foil. The electrolyte consists of 1M $NaClO_4$ (>99%, Sigma-Aldrich) in ethylene carbonate (EC) and dimethyl carbonate (DEC) (1:1 in volume), with 2 vol % fluoroethylene carbonate (FEC) was used. A sodium foil was used as the counter electrode and a glass fiber (GF/D 47, Whatman) was used as the separator. All the operations were conducted in an argon-filled glovebox. The discharge and charge tests were conducted on Neware battery test system (NEWARE, Shen Zhen, China) in a voltage range of 0.01 - 3 V (vs. Na^+/Na) at different current densities at 22 °C. Cyclic voltammetry (CV) tests were performed at different scan rates (0.1 – 1 mV/s) within the voltage range of 0.01 – 3 V. Electrochemical impedance spectroscopy (EIS) was characterized using frequency sweep from 0.001 Hz to 100000 Hz.

Results and discussion

The grand overview of this study is illustrated in the **Fig. 1**. In this top-down approach, we first removed non-lignocellulosic components (protein, starch, fat, and mineral) to obtain pure fiber material called neutral detergent fiber (NDF), which is composed of hemicellulose, cellulose, and lignin. Second, the raw biomass was subjected to a mild chemical treatment to precisely remove hemicellulose to obtain acid detergent fiber (ADF), which is mainly composed of cellulose and lignin. In the chemical-enzymatic fractionation process, two detergent solutions (NDF detergent and ADF detergent) were used to remove the targeted components to obtain the NDF and ADF fractions, respectively. Both the NDF and ADF fractionation processes follow designated programmed procedures, under high temperature (105 °C) and elevated pressure (15 – 20 psi) conditions, with extensive shaking and periodic washing steps[41,42] (more information is available in the experimental section). Last, ADF was treated with harsh H_2SO_4 to dissolve cellulose to obtain pure lignin called Klason lignin. Raw biomass, NDF, ADF, and Klason lignin were subjected to carbonization at 800 °C and 1050 °C in a tube furnace to obtain different hard carbons, which were thoroughly characterized for their structural, surface chemical, and electrochemical properties. We used BSG, which is an agricultural waste, as a model biomass to demonstrate the impact of precursor composition on the carbon properties due to its relatively balanced composition of protein, cellulose, hemicellulose and lignin. The major compositions in BSG are cellulose (23.2 ± 0.2%), hemicellulose (34.0 ± 0.5%), lignin (7.3 ± 0.4%), and other components (35.5 ± 0.5%) (**Fig. S1**). The obtained carbon samples are denoted as "Biomass Fraction_TemperatureC" (e.g. BSG Raw_1050C refers to the carbon directly derived from the raw BSG at 1050 °C). The carbonization yield of each sample is shown in Table S7.

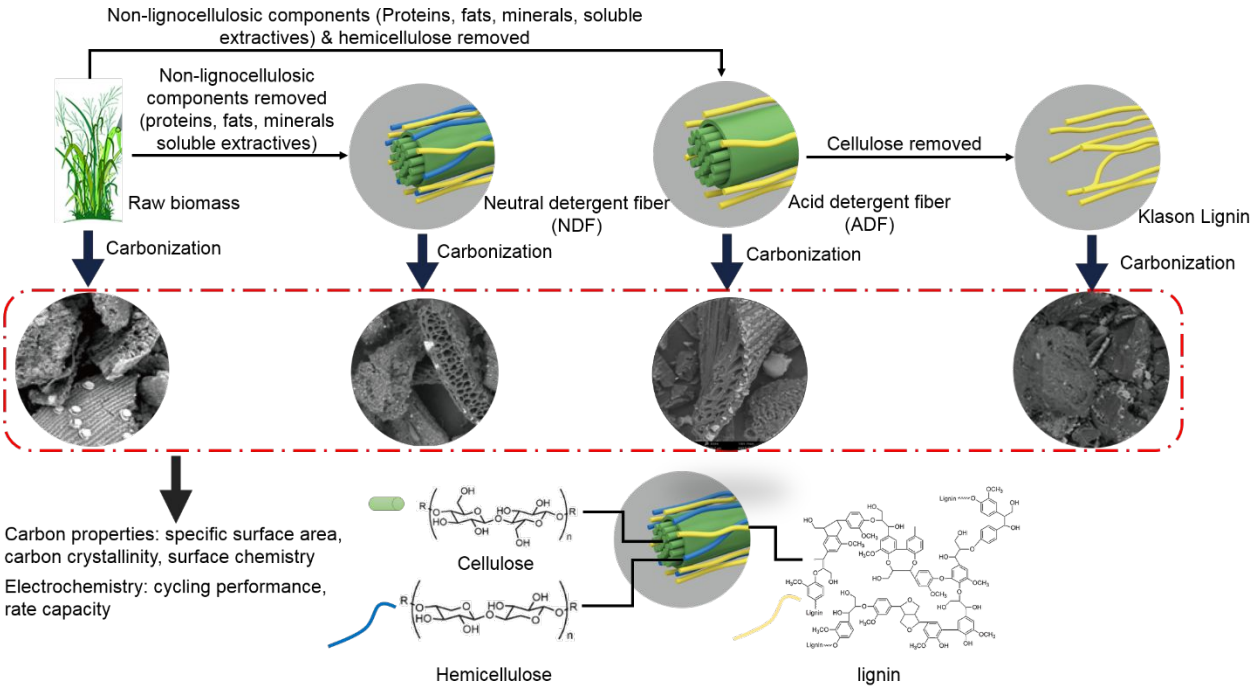

Fig. 1. A schematic diagram illustrating the approach of utilizing the targeted fractionation method to produce different carbon materials for sodium ion battery anodes.

The SEM images in **Fig. 1** show representative microstructures of hard carbons derived from different fractions of BSG: raw, NDF, ADF and lignin. Hard carbons derived from raw BSG by carbonization at 1050 °C contain solid particles with bright color on the carbon surfaces; these particles are typically recognized as metal element containing compounds derived from minerals. As to the carbons derived from NDF, ADF and lignin, solid particles on carbon surfaces diminished, indicating the effective removal of minerals during the chemical-enzymatic treatment. Also, there are more cracking and wrinkles on the carbon surface from the raw BSG, which is a sign of large specific surface area. Comparing the SEM images of hard carbons derived from NDF, ADF and lignin, parallel tube-like structure could be identified in NDF and ADF derived carbons, which could be inherited from the original crystalline cellulose, because both NDF and ADF contain a large amount of cellulose. In contrast, the lignin-derived carbon exhibited a bulky morphology, without the parallel-tube like structure or inter-connected pores. More SEM images of carbons from BSG samples and other biomass can be found in the supplementary information (Fig. S2, S3 and S4). The morphology of lignin-derived carbon aligns well with a previous study by Deng et al[43]. Cellulose and hemicellulose are rich of hydroxyl groups[7,44], which undergo

dehydration readily during carbonization process and, as a result, form a three-dimensional structure with interconnected pores[43].

According to the X-ray diffraction (XRD) results (**Fig. 2a**), the carbon materials derived from raw BSG and NDF are mostly amorphous with only broad reflection peaks at 2θ = 22° and 43°, whereas the ADF and lignin derived carbon materials show a clear peak at 2θ = 22°, indicating a more ordered structure. This result suggests that removing non-lignocellulosic components and hemicellulose leads to more crystalline structure of the derived carbon materials. The critical carbon structure parameters, average lateral sizes (L_a), stacking heights (L_c) and interlayer spacing (d_{002}) were estimated based on the XRD patterns (**Table 1**). The d_{002} in the BSG ADF_1050C and BSG Lignin_1050C were 3.86 and 3.84 Å, respectively. The numbers are greater than that of BSG Raw_1050C and BSG NDF_1050C, indicating the removal of hemicellulose helped to expand the interlayer spacing between carbon sheets. Compared to hemicellulose which decomposes around 210 - 325°C, cellulose and lignin decompose at higher temperatures (310 - 400°C for cellulose, and 250 - 900°C for lignin)[45], thus removing hemicellulose may result in delayed formation of chars to a higher temperature, which consequently hinders the re-organization of carbon sheets, leaving a larger interlayer spacing[46]. HRTEM images of carbonized BSG from different fractions were also collected to estimate the d_{002} and confirm XRD results (Fig. S5 and S6). Although there are minor differences in terms of the calculated numbers, the results showed the same trend among these four samples (Table S1).

Fig. 2b compares carbons derived from different fractions using Raman spectroscopy. The two characteristic carbon bands at 1340 cm^{-1} and 1585 cm^{-1} are ascribed to the disordered sp^3 carbon (D band) and the ordered sp^2 carbon (G band), respectively. The peak intensity ratio (I_G/I_D) between the G band and D band usually reflects the degree of order in turbostratic carbon. The I_G/I_D ratio of raw biomass, NDF, ADF, and lignin from three biomasses (BSG, grape pomace, and walnut shell) were plotted in the **Fig. 2c**. Within each biomass, the I_G/I_D ratios generally follow the same trend among different fractions. The raw biomass resulted in a relatively high I_G/I_D value, while the NDF fraction (after removal of proteins, lipids, extractives, minerals) showed a decreased I_G/I_D value. The decrease is probably attributed to the removal of minerals containing transition metals such as Fe and Ni, which could serve as graphitization catalysts during carbonization[47,48]. A drastic increase of I_G/I_D was found from NDF to ADF by removing

hemicellulose. Hemicellulose is an amorphous polymer made of heterogeneous monosaccharide unites (arabinoxylans, arabinogalactans, β-glucans, etc)[49]. After the thermal depolymerization of hemicellulose into a variety of monosaccharides, thermal degradation and ring rearrangement occur. Due to the differences in the thermal stability of each monosaccharide unit, the thermal degradation of hemicellulose takes place in a wide temperature range, as indicated by the weight loss curve using TGA in a previous work[50]. The carbon rearrangement could be thus hindered and lead to a low degree of sp^2 carbons. On the other hand, the decomposition of cellulose takes place in a narrower temperature range (310 ~ 400 °C)[45], because cellulose is composed of one single monomer, β-glucose. Such a uniform composition may facilitate the recombination of carbon rings into carbon sheets with sp^2 arrangements. Further removal of cellulose then decreases the I_G/I_D ratio, because lignin is a highly thermo-resistant component due to rich cross-linking[37]. With the slow kinetics of thermal decomposition, the formation of sp^2 structure could be substantially suppressed.

The specific surface area of BSG derived carbons were studied using the N_2 adsorption/desorption isotherms (**Fig. 2d**) and the results were summarized in the **Table 1**. The BSG raw_1050C showed the largest surface area (462.5 m^2/g) compared to carbons derived from the NDF, ADF and lignin fractions. According to the pore size distribution plot in the **Fig. 2e**, the large surface area of the BSG raw_1050C is contributed by micro-meso pores that are less than 5 nm. Those pores are typically generated during self-activation processes due to the natural presence of potassium, zinc and phosphate in the biomass[51,52]. After removing minerals, the specific surface area of lignocellulosic fractions (NDF, ADF, lignin) significantly decreased, probably due to the diminishment of micro-meso pores. The reduced specific surface area has been reported crucial for the sodium battery chemistry by reducing electrode-electrolyte side reactions and improving Coulombic efficiency[53].

The above characterization results have unambiguously demonstrated that different fractions of biomass can lead to variations in the morphological and structural characteristics of the derived carbon materials. The NDF fraction, which are rich in amorphous hemicellulose, result in less sp^2 bonded carbons and reduced interlayer spacing (d_{002}) of the derived carbon materials. In contrast, the ADF, which is rich in crystalline cellulose with no hemicellulose, leads to more sp^2 bonded carbons, expanded interlayer spacing, and reduced specific surface area.

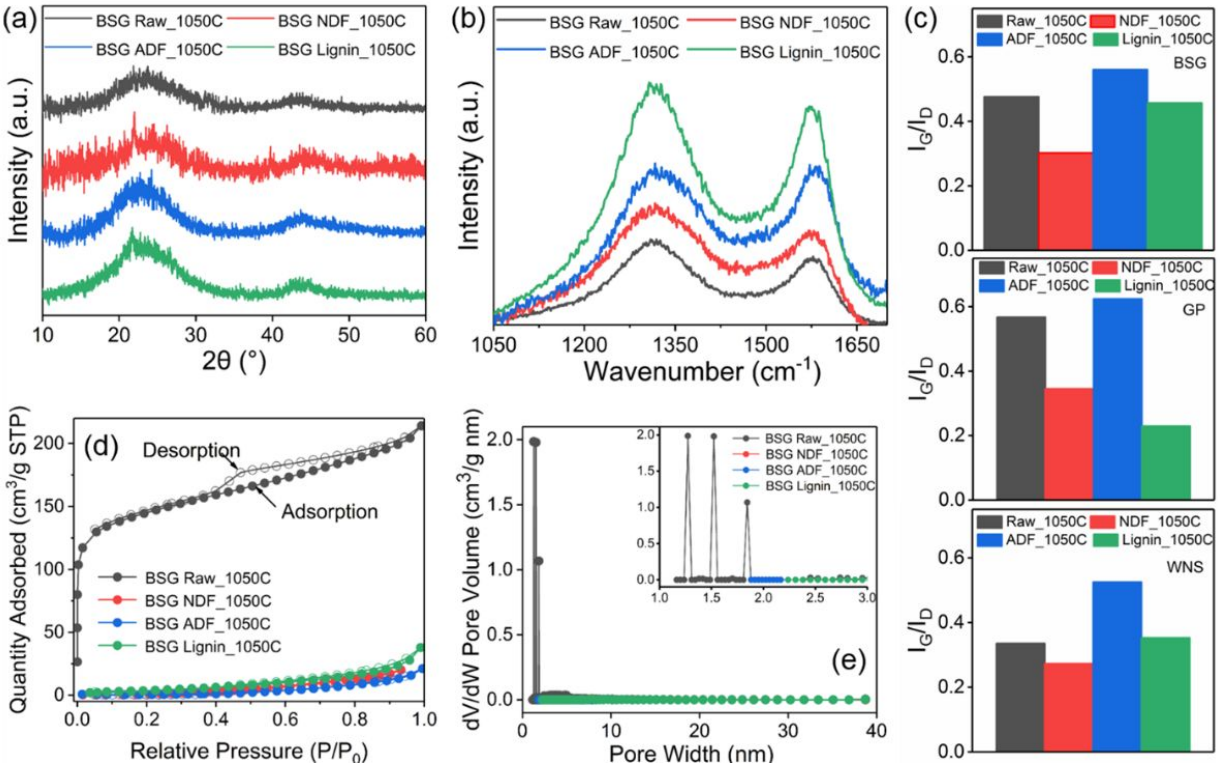

Fig. 2. (a) XRD patterns of carbon materials derived from BSG (b) Raman spectrum of carbon materials derived from different fractions of BSG at 1050 °C. (c) I_G/I_D ratio of carbon materials derived from BSG, GP and NDF at 1050 °C. (d) N_2 adsorption/desorption isotherms. (e) Pore size distribution.

Table 1. A comparison of carbon structures obtained from different fractions of BSG.

Sample name	BET (m^2/g)	d_{002} (Å)	L_a (Å)	L_c (Å)	I_G/I_D
BSG Raw_1050C	462.5	3.76	24.89	8.04	0.476
BSG NDF_1050C	3.6	3.75	24.42	9.38	0.302
BSG ADF_1050C	1.6	3.86	19.41	10.10	0.560
BSG lignin_1050C	15.8	3.84	40.11	8.52	0.457

The surface chemistry of carbons was quantified using X-ray photoelectron spectroscopy (XPS) to reveal the surface functional groups. **Fig. 3a~3d** compares the C 1s high-resolution XPS spectra

of the carbons derived from different fractions of BSG. The C 1s spectra were deconvoluted into C-C sp^2 bonds (284.6 eV), C-O bonds (286.4 eV), C=O bonds (287.7 eV) and C-OOH bonds (289.7 eV), respectively[54]. The results showed that the BSG ADF_1050C contains the most abundant C-C sp^2 bonds (47%), which aligns with its highest I_G/I_D peak ratio in the Raman spectrum. The C-C sp^2 group are responsible for constituting the graphitic carbon sheets, which stacked with each other to form interlayers allowing for sodium ion intercalation[55]. Many studies also suggested that surface functional groups of hard carbons play vital roles during sodiation and desodiation process[45,56]. Kang et al found that the presence of oxygen on carbon surface significantly improved sodium intercalation, which may be attributed to the improved sodium affinity through the O-Na interactions[57]. In this study, all the samples possess similarly large amount of C=O and C-O bonds, suggesting desirable sodium affinity. The BSG Lignin_1050C contains the highest fraction of C-OOH bond (12%), which is associated with extensive cross-linking between the phenylpropane in lignin and the resulting thermal stability[35]. The rich C-OOH bonds in the BSG lignin_1050C could be detrimental to its electrochemical performance because the occupancy of -OH group leaves less free volume for sodium migration[57], and suppressed sodium diffusivity. The O 1s spectrums (Fig. S7) suggest that the BSG NDF_1050C sample is rich of C-O-H bond (Table S2), which may also result in its low sodium ion diffusivity (Table S5).

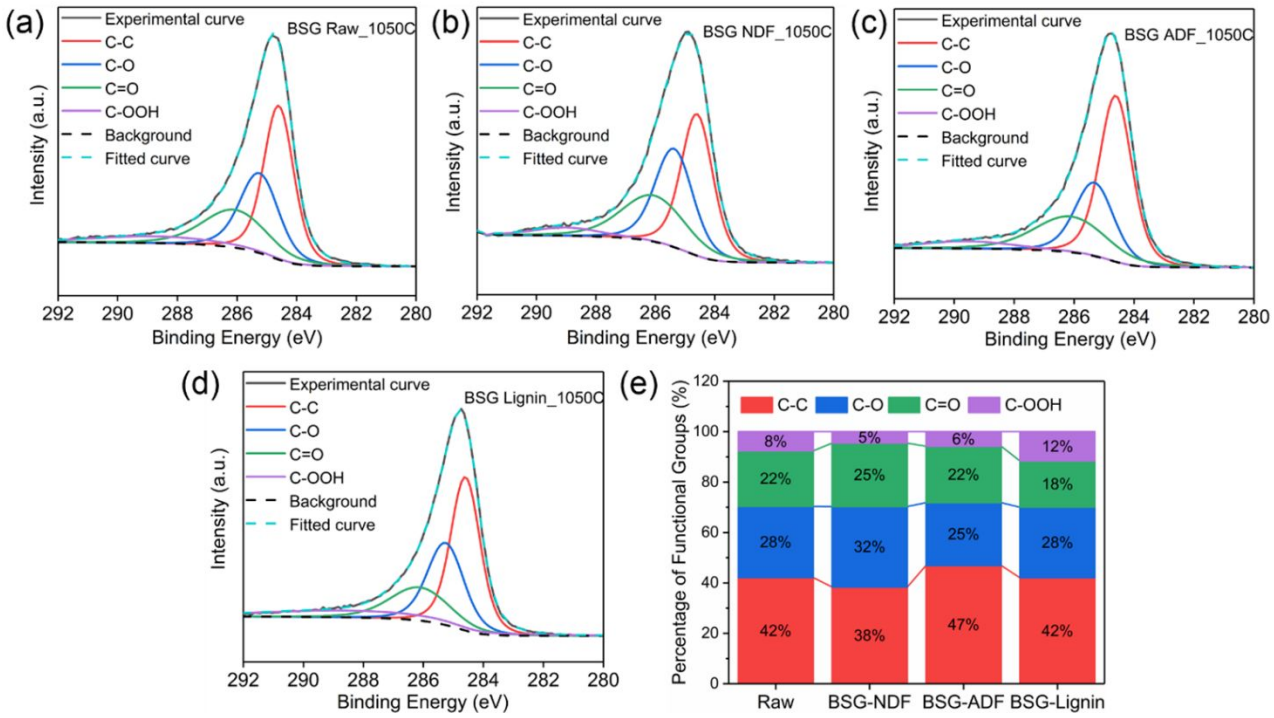

Fig. 3. Characterization and comparison of hard carbon materials derived from different fractions. (a) high-resolution C 1s XPS spectrum of BSG raw_1050C. (b) high-resolution C 1s XPS spectrum of BSG NDF_1050C. (c) high-resolution C 1s XPS spectrum of BSG ADF_1050C. (d) high-resolution C 1s XPS spectrum of BSG lignin_1050C. (e) Percentage of functional groups in carbons derived from different fractions of BSG.

The electrochemical measurements show that the carbon derived from fractionated BSG exhibited drastically improved electrochemical performance than the carbon derived from the raw BSG. The sodium ion battery half cells were assembled using 1M $NaClO_4$ in EC/DMC (1:1 in volume ratio) as the electrolyte, sodium metal as the reference and counter electrode, and the derived carbon as the working electrode. A direct comparison of electrochemical performance between the BSG ADF_1050C and BSG raw_1050C is shown in the **Fig. 4**. At the current density of 100 mA g^{-1} (0.4 C, 1C = 250 mA g^{-1}), the reversible charging capacity of BSG raw_1050C was only 35 mAh g^{-1} (**Fig. 4a**), whereas the BSG ADF_1050C is increased by four folds to 184 mAh g^{-1} (**Fig. 4b**). The low reversible capacity of BSG raw_1050C could be attributed to its large specific surface area that leads to extensive side reactions between the electrochemical active materials and electrolyte[58]. The Columbic efficiency (CE) comparison (**Fig. 4c**) shows that the BSG ADF_1050C started with 72.0% and it readily reached 99.3% in the 4^{th} cycle, whereas the BSG raw_1050C started with 69.7% and took 53 cycles to reach 99.3%. The differences in CE% during cycling confirmed that there was more irreversible capacity loss in BSG raw_1050C due to the larger surface area. The BSG ADF_1050C also presented significantly lower average charging/discharging voltages than the BSG raw_1050C **(Fig. 4d)**, indicating greater power density and energy density as an anode in future full cells, as well as promising capability to maintain a low degree of polarization[59,60]. The lowered voltage is associated with the carbon structure differences between the BSG ADF_1050C and BSG raw_1050C. According to the most acceptable "house of cards" model for sodium storage in hard carbons[61], the sloping potential profile at the high potential range is related to the intercalation of Na^+ into the carbon interlayer, and the plateau region at the low potential range corresponds to the adsorption of the Na^+ into the voids between randomly stacked layers[62]. For Na^+, an expanded interlayer spacing has been suggested necessary for intercalating Na^+ [63]. In this work, the d_{002} of BSG ADF_1050C (3.86 Å) is larger than that of the BSG raw_1050C (3.76 Å). The expanded d_{002} lowered the energy penalty for Na^+ to enter and diffuse in the carbon matrix, which has been validated by the theoretical DFT

calculation[64]. The charge-discharge curves of BSG NDF_1050C and BSG Lignin_1050C (Fig. S10) also suggest the determining role of d_{002} on plateau capacity at low voltages. The BSG NDF_1050C sample (d_{002} = 3.75 Å) exhibited almost no plateau capacity while the BSG Lignin_1050C (d_{002} = 3.84 Å) exhibited over 50% of plateau capacity. In addition to the d_{002}, a smaller specific surface area was also reported to favor sodium ion storage[53]. The electrochemical impedance spectroscopy (EIS) was performed to evaluate the charge transfer resistance at the anode (**Fig. S9**). The charge transfer resistance (R_{ct}) of BSG raw_1050C sample is significantly lower than other samples, probably due to its large content of mineral unremoved. BSG ADF_1050C and BSG Lignin_1050C exhibited much larger charge transfer resistance (246.8 Ω & 285.9 Ω), which are within the typical range for biomass-derived hard carbon materials[65] (Table S4). However, the charge transfer resistance of BSG NDF_1050C reached very high value at 739.2 Ω, which could be detrimental to its charge transfer efficiency and thereby significantly lower its rate capability.

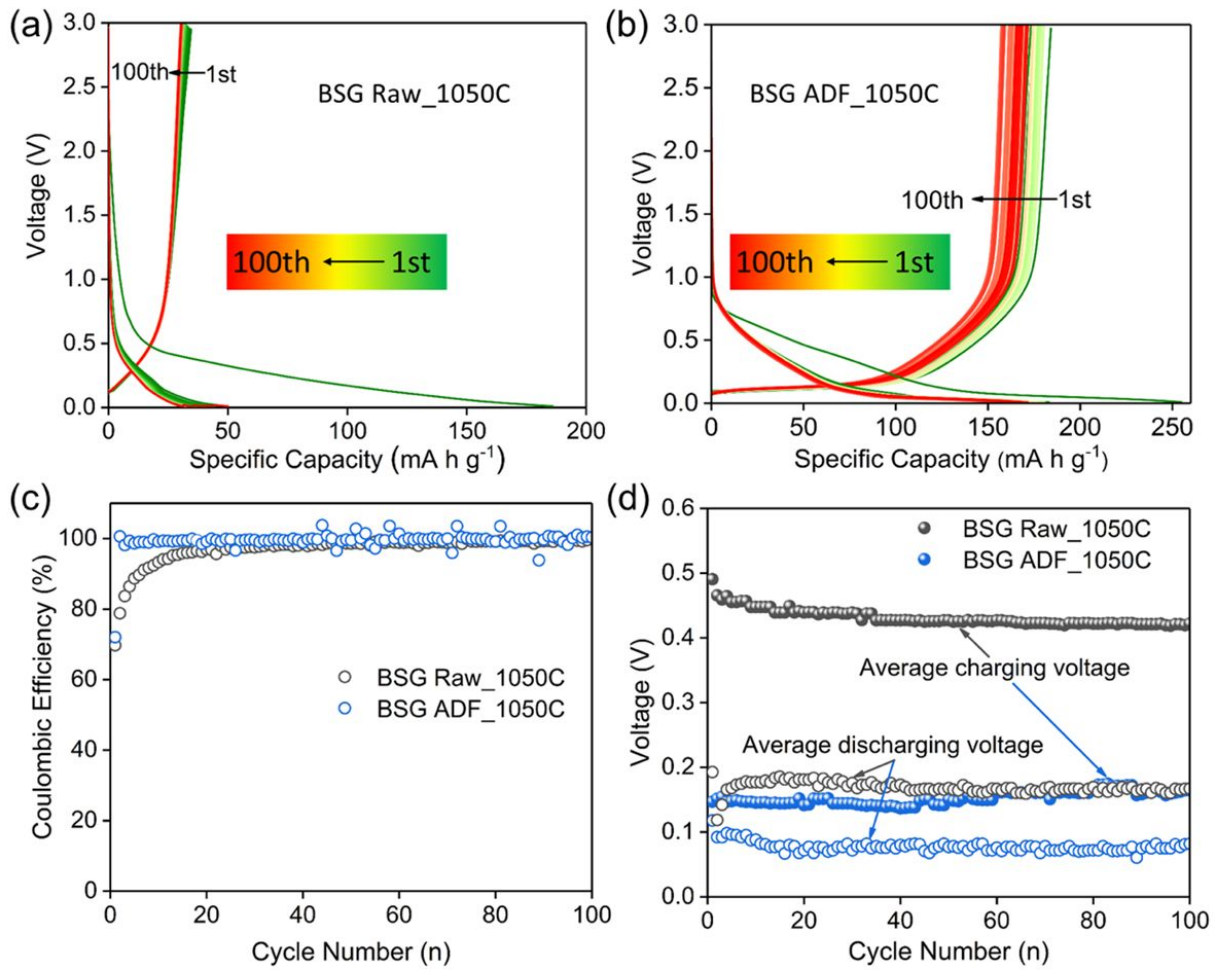

Fig. 4. Comparison of electrochemical performance of carbon materials derived from raw BSG and ADF BSG at 1050 °C. (a) Charge-discharge cycles (100 mA g^{-1}, 100 cycles) of raw BSG; (b) Charge-discharge cycles (100 mA g^{-1}, 100 cycles) of ADF BSG; (c) Coulombic efficiency (CE%) of raw BSG and ADF BSG. (d) Average charging voltage (V_c) and average discharging voltage (V_d).

The rate capability and cycling performance of carbons derived from the raw BSG and different fractions of BSG are shown in the **Fig. 5a**. In terms of the rate capability, BSG ADF_1050C showed the best performance than other samples, because of its highest amount of sp^2 bonded domains that are accessible for intercalation, expanded d_{002} interlayer spacing that minimizes sodium storage energy barrier[66], and the lowest content of C-OOH bonds that facilitate sodium diffusion. At a low current density (50 mA g^{-1}), both BSG ADF_1050C and BSG lignin_1050C showed premium reversible capacity (184 mA g^{-1} for BSG ADF_1050C and 177 mA g^{-1} for BSG lignin_1050C) , while the capacity of BSG Lignin_1050C decays progressively with increasing current density, which could be related to its greater amount of C-OOH bonds than BSG ADF_1050C. Due to the structural difference, BSG lignin_1050C may also suffer more stress during the insertion and extraction of Na^{+}[67].

Fig. 5b, 5c display the differential capacity profiles (dQ/dV) of the BSG raw_1050C and BSG ADF_1050C at the current density of 100 mA g^{-1}. The BSG ADF_1050C presented the intercalation peak and de-intercalation peak at very low voltages, 0.01 - 0.05V and 0.1 - 0.2 V, respectively. These two peaks shifted mildly after 100 cycles, indicating desirable structural stability. As to the BSG raw_1050C, the Na^{+} plating process involved an extensive side reaction, and the intercalation/de-intercalation peaks were not as sharp as those of the ADF BSG_1050C. This observation is consistent with the results represented in **Fig. 4a** that the BSG raw_1050C mostly exhibits non-plateau capacity (i.e., more slopy voltage profiles).

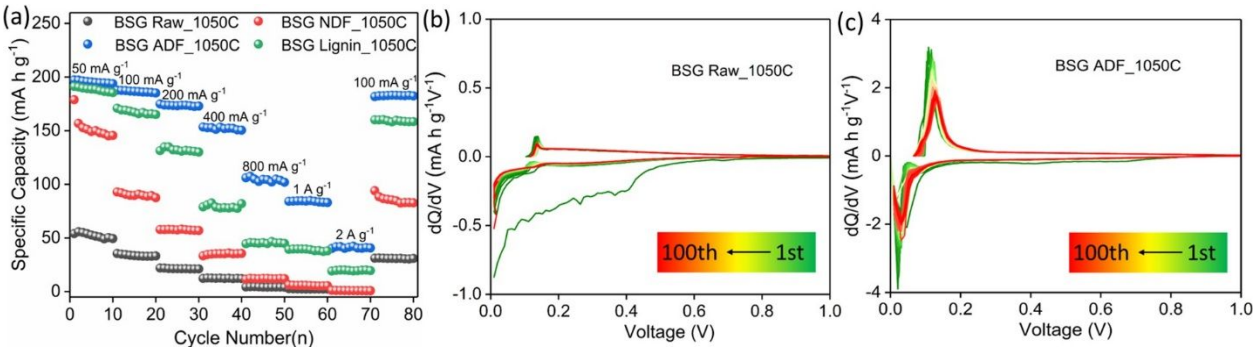

Fig. 5. Comparison of electrochemical performance of carbon materials derived different fractions of BSG at 1050 °C. (a) Rate capability (50, 100, 200, 400, 800, 1000, 2000, 100 mA g^{-1}), 10 cycles at each current density. (b) dQ/dV curve (100 mA g^{-1}, 100 cycles) of carbon materials derived from raw BSG at 1050°C. (c) dQ/dV curve (100 mA g^{-1}, 100 cycles) of carbon materials derived from ADF BSG at 1050°C.

Sodium storage and transportation mechanisms in different BSG fractions were further investigated using cyclic voltammetry (CV) (Fig. 6). In **Fig. 6a**, all the samples were measured at a scanning rate of 0.2 mV/s. Sharp anodic and cathodic peaks at low voltages were found in the BSG ADF_1050C sample, suggesting the formation of intercalation compounds in the plateau region[68]. Two hypotheses have been proposed to explain sodium storage in hard carbon materials. The classic house of cards model suggests that the plateau capacity at low voltages is attributed to intercalation and the sloping capacity is due to adsorption[61]. However, the house of cards model was recently challenged in a recent work[66]. To further understand the sodium storage mechanisms in the sloping and plateau regions, the sodiation and desodiation kinetics of BSG ADF_1050C sample were investigated using the varying rate CV scanning method. Based on curve-fitting, the CV data can be used to interpret whether the sodium transport occurs at surface or bulk. The surface mass transport refers to sodium adsorption and the bulk mass transport indicates sodium intercalation[15,69,70]. Following the previous described method, CV curves of BSG ADF_1050C sample were collected at five different scanning rates (0.1, 0.2, 0.3, 0.5 and 1mV/s), shown in **Fig 6b**. The peak currents at anodic and cathodic peaks in the plateau region are noted as P and P', while the currents in the sloping region were noted as S and S'. The mathematical correlation between currents (i) and scan rates (v) were studied using the curve fitting[69] (1).

$$i = a \times v^{b} \quad (1)$$

Typically, smaller b value that close to 0.5 indicates a bulk mass transportation with a slow kinetics. On the other hand, if the b value is close to 1, it indicates a surface mass transportation and fast kinetics[69,70]. In this work, the b value was found to be close to 0.5 at in the plateau region and close to 1 in the sloping region **(Fig. 6c)**. Therefore, the "house of cards" model[61] is more appropriate to describe the sodium storage in the hard carbons obtained in this study. This result aligns with most of recent works that studied sodium-hard carbon interactions[15,71–73].

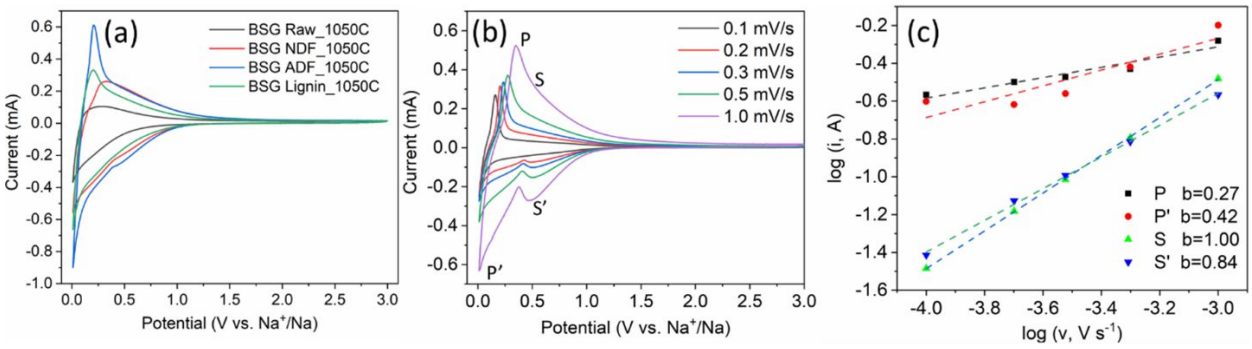

Fig. 6. (a) The comparison of CV curves (0.2 mV/s) of carbons from different BSG fractions. (b) CV curves of BSG ADF_1050C collected with varying scan rates at 0.1 mV/s, 0.2 mV/s, 0.3 mV/s, 0.5 mV/s and 1mV/s. (c) Plots of log(i) versus log(v) for BSG ADF_1050C sample and the corresponding linear fitting.

The ADF from two additional types of agricultural biomass, grape pomace (GP), and walnut shell (WNS), were also prepared as anode materials for sodium ion batteries. At both two temperatures being selected in this study (800 °C and 1050 °C), the carbon anodes derived from the ADF showed a better specific capacity and cycling stability than the carbon anodes derived from the raw biomass (**Fig. 7**). These results confirmed that fractionation of biomass into ADF could be used as a common strategy to improve the specific capacity or cycling performance for other types of biomass in the present study. It was also found that the ADFs from different types of biomass resulted in different electrochemical performances. The carbon anodes prepared from WNS ADF_1050C displayed the highest reversible capacity (263 mAh g^{-1} at 100 mA g^{-1}), while the BSG ADF_1050C showed the lowest reversible capacity (184 mAh g^{-1} at 100 mA g^{-1}). The capacity differences among ADF fractions could be related to three aspects: 1) the cellulose : lignin ratios in these three types of biomass vary distinctively (**Fig. S1**), which is about 3:1 for the BSG, 1:1.5 for the GP and 1:1 for the WNS; 2) the ratios among each type of lignin monomer (G:H:S)

vary among different biomass, while their effects on the resulting carbon properties have not been understood; 3) the molecular weight or chain length of cellulose from different types of biomass are also different[26]. It is interesting that the both the WNS ADF_800C and the WNS ADF_1050C did not significantly improve the specific capacity compared to WNS Raw_800C and WNS Raw_1050C, respectively. In fact, the chemical composition of WNS ADF is very similar to the raw WNS, with the non-lignocellulosic components as low as 9%. In comparison, the non-lignocellulosic components are 35% for BSG and 50% for GP, respectively (**Fig. S1**). Featured by its high lignocellulosic weight percentage, the raw WNS without any lignocellulosic component removal as well as many other nutshells have been reported as excellent carbon anode precursors for sodium ion batteries [45,74]. When comparing the cycling performance between WNS ADF_800C and WNS Raw_800C (**Fig. 7c**), WNS ADF_800C presented slightly better cycling stability at 40 cycles while the difference becomes prominent at 100 cycles (**Fig. S8**), indicating that the removal of trace amount of impurities and hemicellulose would also help improve the electrode stability. On the other hand, the theoretical highest capacity of turbostratic carbon anodes for sodium ion batteries have been reported in the range between 300 mAh g^{-1} to 500 mAh g^{-1}, depending on the d_{002} and the average number of graphitic sheets (n)[71]. Since it is not realistic that all of the carbons form regular graphic-like sheet structure in turbostratic carbons, the highest capacities reported in previous studies were around 300 mAh g^{-1} [72]. In this study, the specific capacity of WNS ADF_1050C also achieved a high capacity of 296 mAh g^{-1} at 50 mA g^{-1}, as shown in the **Fig. 7f**.

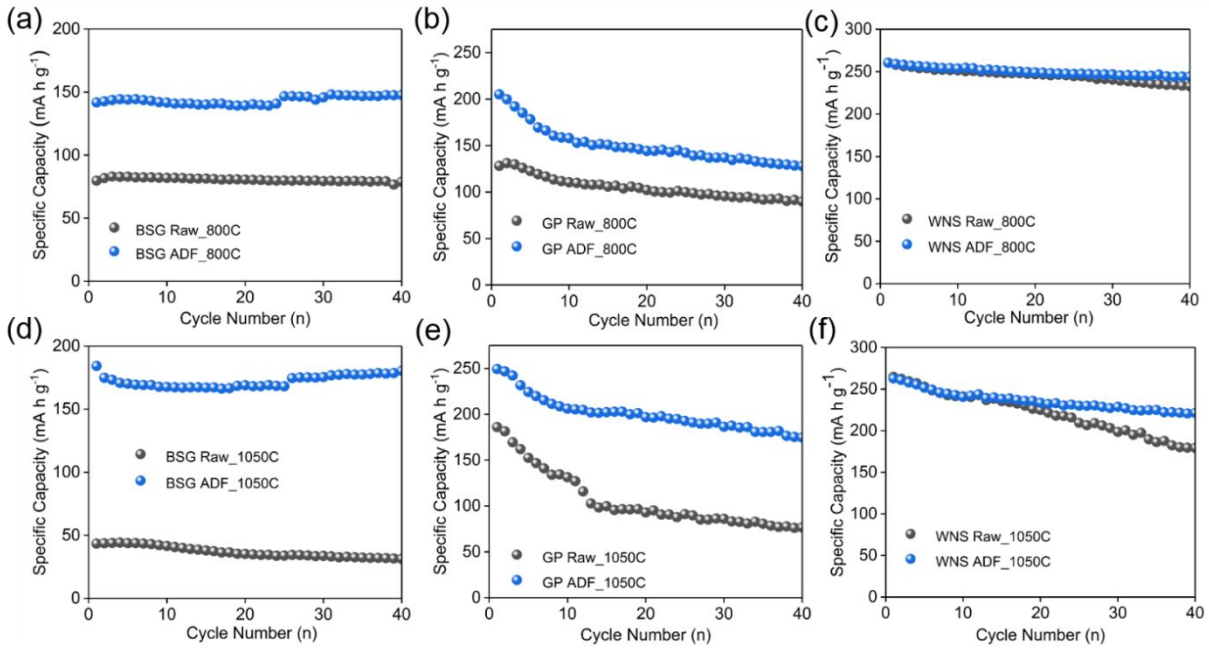

411 **Fig. 7.** Comparison of the electrochemical performance (100 mA g^{-1}, 40 cycles) of carbon
412 materials derived from different fractions (Raw vs. ADF), across carbonization temperatures &
413 biomass types. (a) BSG 800 °C (b) GP 800 °C (c) WNS 800 °C (d) BSG 1050 °C (e) GP 1050 °C
414 (f) WNS 1050 °C.

415 A long cycling test was performed at 50 mA g^{-1} for the ADF fractions from BSG, GP and WNS
416 (**Fig. 8**). The WNS ADF_1050C exhibited the highest reversible specific capacity (296 mAh g^{-1})
417 among the three. As discussed above, the intrinsic differences in terms of the cellulose/lignin ratio,
418 lignin monomer composition, as well as the molecular weight of cellulose could be the key factors
419 resulting in the different electrochemical performances. All the ADF fractions tested in this study
420 showed acceptable retention of specific capacity after 200 cycles (> 80%), and the WNS
421 ADF_1050C showed the highest capacity retention of 86.4%. Similar or slightly lower capacity
422 retention numbers were reported using hard carbon as sodium ion battery anodes[72,75]. The early
423 stage irreversible capacity loss is commonly from the SEI formation and electrolyte
424 decomposition[76], while the later stage capacity loss may be attributed to side reactions with binders
425 being used for carbon materials[77]. It has also been noted that the both GP Raw and GP ADF
426 samples are subjected to substantial capacity delay during the electrochemical cycles, which could
427 be attributed to their ultra-high lignin contents of 52% (**Fig. S1**). As a hard carbon precursor, lignin
428 tends to form carbon materials with high surface area and large number of open pores, which are
429 typically responsible for the irreversible capacity[53].

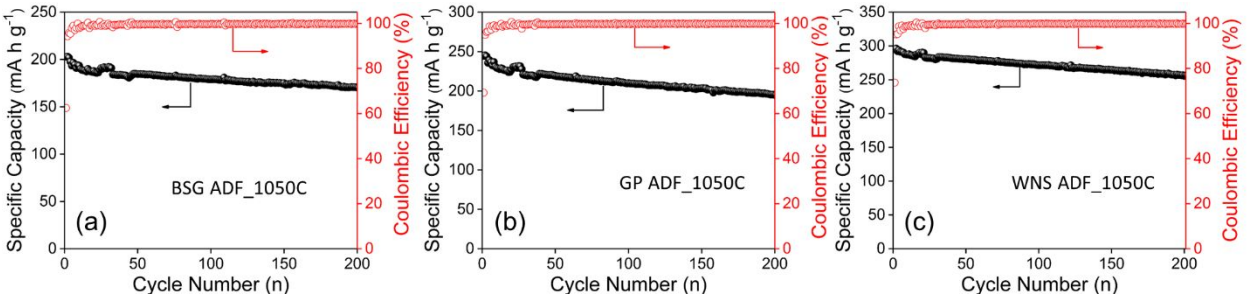

430

431 **Fig. 8.** Comparison of the long cycling performance (50 mA g^{-1}, 200 cycles) of carbon materials
432 derived from the same fraction (ADF) using same temperature (1050°C) across different biomass
433 types. The black lines represent the specific capacity (Y1 axis in the left), and the red dots are the
434 coulombic efficiency (Y2 axis in the right). (a) BSG ADF_1050C (b) GP ADF_1050C (c) WNS
435 ADF_1050C.

Conclusions

Manipulating the biomass components for carbonization will potentially transform the valorization of biomass wastes for rechargeable batteries. Such a bioprocessing-guided approach has not been widely applied in the current hard carbon research, which has underestimated the large tunability of biomass-derived carbons for sodium ion batteries. In this work, we developed a top-down approach to precisely manipulate the biomass composition, for the purposes of investigating the effect of each component on the structural and electrochemical properties of derived carbon materials. By removing different components from biomass, we found that the microstructure, degree of graphitization, lattice parameters and surface functional groups of the derived carbon materials can be finely controlled. For all three types of biomass selected in this study, the ADF fraction exhibited promising electrochemical performance. For BSG and GP, using the fractionated ADF as hard carbon precursors lead to a drastic increase of the reversible capacity. For WNS, the ADF fraction derived hard carbon exhibited more stable cycle stability. Compare to other most recent work, the electrochemical performance of this study is among the first tier in terms of reservable capacity, Columbic efficiency and cycling stability (Fig. S11 & Table S6). The excellent electrochemical performance of the ADF fraction-derived carbon is associated with more intercalation sites, lower sodium intercalation energy barrier and suppressed side reactions, which are directly associated with their structural features, including greater amount of sp^2 bonded carbon, lower surface area and larger interlayer spacing (d_{002}). The finding indicates that, the electrochemical performance of biomass-derived carbon materials in sodium ion battery can be remarkably improved by proper fractionation to remove undesirable components or selecting biomass precursors with targeted chemical composition. With the rapidly increasing demand for rechargeable batteries, biomass-derived carbon materials are regarded as promising alternatives for energy storage, which address a list of raising concerns associated with cost efficiency, environmental impacts, life cycles and supply chain sustainability. By unraveling the profound impact of biomass composition, this work provides fundamental insights into producing robust, sustainable and cost-effective biomass-derived carbon materials for energy storage applications.

Acknowledgements

Y.F. and H.H. acknowledge the support from the Virginia Agriculture Experiment Station and the Hatch Program of the National Institute of Food and Agriculture (NIFA), USDA. L.T. and F.L. acknowledge the support from the Virginia Tech Institute for Critical Technology and Applied Science Junior Faculty Award, and the Virginia Tech Department of Chemistry Startup Funds. The authors would like to thank Dr. Weinan Leng for the assistance in collecting XPS and Raman data, Dr. Chixia Tian and Anyang Hu for performing the SEM measurements, Dr. Hengjian Wang for the biomass fractionation, Zhengrui Xu for preparing the electrolyte, Anyang Hu for the X-ray analysis and Weijie Zhang for the image editing. This work used shared facilities at the Virginia Tech National Center for Earth and Environmental Nanotechnology Infrastructure (NanoEarth), a member of the National Nanotechnology Coordinated Infrastructure (NNCI), supported by NSF (ECCS 1542100).

Author Contribution

H.H. and F.L. conceived and led the project. Y.F. and L.T. performed materials synthesis, characterization, and electrochemical measurements, and contributed equally to this work. Y.H. and Q.J. performed the compositional analysis. Z.Z. and Y.Z. collected and analyzed the BET and XRD data. Q.H. assisted the materials synthesis and electrochemical measurements. M.L. and C.K. performed the HRTEM analysis. Y.F., L.T., F.L., and H.H. analyzed all data and wrote the manuscript with assistance from all the coauthors.

Conflict of Interest

The authors declare no conflict of interest.

References

1 H. Ying and W. Q. Han, *Adv. Sci.*, , DOI:10.1002/advs.201700298.

2 N. Yabuuchi, K. Kubota, M. Dahbi and S. Komaba, *Chem. Rev.*, 2014, **114**, 11636–11682.

3 J. R. Rodriguez, S. B. Aguirre and V. G. Pol, *J. Power Sources*, 2019, **437**, 226851.

4 W. Luo, F. Shen, C. Bommier, H. Zhu, X. Ji and L. Hu, *Acc. Chem. Res.*, 2016, **49**, 231–240.

5 W. Qian, F. Sun, Y. Xu, L. Qiu, C. Liu, S. Wang and F. Yan, *Energy Environ. Sci.*, 2014, **7**, 379–386.

6 Z. Li, Z. Xu, X. Tan, H. Wang, C. M. B. Holt, T. Stephenson, B. C. Olsen and D. Mitlin, *Energy Environ. Sci.*, 2013, **6**, 871–878.

7 W. Wang, Y. Sun, B. Liu, S. Wang and M. Cao, *Carbon*, 2015, **91**, 56–65.

8 Y. Huang, Z. Lin, M. Zheng, T. Wang, J. Yang, F. Yuan, X. Lu, L. Liu and D. Sun, *J. Power Sources*, 2016, **307**, 649–656.

9 J. H. Um, C.-Y. Ahn, J. Kim, M. Jeong, Y.-E. Sung, Y.-H. Cho, S.-S. Kim and W.-S. Yoon, *RSC Adv.*, 2018, **8**, 32231–32240.

10 V. Chaturvedi and P. Verma, *3 Biotech*, 2013, **3**, 415–431.

11 M. Gao, S. Y. Pan, W. C. Chen and P. C. Chiang, *Mater. Today Energy*, 2018, **7**, 58–79.

12 Y. Shen, *J. Agric. Food Chem.*, 2017, **65**, 995–1004.

13 H. Huang, Z. Jiao, Z. Shu and Y. Zeng, in *Proceedings of the 2nd International Conference on Green Materials and Environmental Engineering*, Atlantis Press, Paris, France, 2015, pp. 174–178.

14 D. Yoon, J. Hwang, W. Chang and J. Kim, *ACS Appl. Mater. Interfaces*, 2018, **10**, 569–581.

15 Z. Zhu, F. Liang, Z. Zhou, X. Zeng, D. Wang, P. Dong, J. Zhao, S. Sun, Y. Zhang and X. Li, *J. Mater. Chem. A*, 2018, **6**, 1513–1522.

16 A. Kumar and H. M. Jena, *Results Phys.*, 2016, **6**, 651–658.

17 K. Kim, D. G. Lim, C. W. Han, S. Osswald, V. Ortalan, J. P. Youngblood and V. G. Pol, *ACS Sustain. Chem. Eng.*, 2017, **5**, 8720–8728.

18 H. Zhu, F. Shen, W. Luo, S. Zhu, M. Zhao, B. Natarajan, J. Dai, L. Zhou, X. Ji, R. S. Yassar, T. Li and L. Hu, *Nano Energy*, 2017, **33**, 37–44.

19 W.-J. Liu, H. Jiang and H.-Q. Yu, *Energy Environ. Sci.*, , DOI:10.1039/c9ee00206e.

20 X. Dou, I. Hasa, M. Hekmatfar, T. Diemant, R. J. Behm, D. Buchholz and S. Passerini, *ChemSusChem*, 2017, **10**, 2668–2676.

21 S. V. Vassilev, D. Baxter, L. K. Andersen and C. G. Vassileva, *Fuel*, 2010, **89**, 913–933.

22 C. Tang, Y. Chen, J. Liu, T. Shen, Z. Cao, J. Shan, C. Zhu and H. Ying, *Ind. Crops Prod.*, 2017, **95**, 383–392.

23 P. Tsapekos, P. G. Kougias, H. Egelund, U. Larsen, J. Pedersen, P. Trénel and I. Angelidaki, *Anaerobe*, 2017, **46**, 131–137.

24 S. S. Hassan, G. A. Williams and A. K. Jaiswal, *Bioresour. Technol.*, 2018, **262**, 310–318.

25 Y. Zheng, J. Zhao, F. Xu and Y. Li, *Prog. Energy Combust. Sci.*, 2014, **42**, 35–53.

26 O. A. Battista, *Ind. Eng. Chem. Anal. Ed.*, 1944, **16**, 351–354.

27 S. Wang, B. Ru, H. Lin and W. Sun, *Fuel*, 2015, **150**, 243–251.

28 J. Baruah, B. K. Nath, R. Sharma, S. Kumar, R. C. Deka, D. C. Baruah and E. Kalita, *Front. Energy Res.*, 2018, **6**, 141.

29 G. Dorez, L. Ferry, R. Sonnier, A. Taguet and J.-M. M. Lopez-Cuesta, *J. Anal. Appl. Pyrolysis*, 2014, **107**, 323–331.

30 W. Mu, H. Ben, A. Ragauskas and Y. Deng, *Bioenergy Res.*, 2013, **6**, 1183–1204.

31 S. rong Wang, T. Liang, B. Ru and X. juan Guo, *Chem. Res. Chinese Univ.*, 2013, **29**, 782–787.

32 A. Jensen, K. Dam-Johansen, M. A. Wójtowicz and M. A. Serio, *Energy and Fuels*, 1998,

12, 929–938.

33 J. Hoekstra, A. M. Beale, F. Soulimani, M. Versluijs-Helder, J. W. Geus and L. W. Jenneskens, *J. Phys. Chem. C*, 2015, **119**, 10653–10661.

34 C. Liu, H. Wang, A. M. Karim, J. Sun and Y. Wang, *Chem. Soc. Rev.*, 2014, **43**, 7594–7623.

35 V. Pasangulapati, K. D. Ramachandriya, A. Kumar, M. R. Wilkins, C. L. Jones and R. L. Huhnke, *Bioresour. Technol.*, 2012, **114**, 663–669.

36 J. Deng, M. Li and Y. Wang, *Green Chem.*, 2016, **18**, 4824–4854.

37 X. Zhou, W. Li, R. Mabon and L. J. Broadbelt, *Energy Technol.*, 2017, **5**, 52–79.

38 O. Fromm, A. Heckmann, U. C. Rodehorst, J. Frerichs, D. Becker, M. Winter and T. Placke, *Carbon*, 2018, **128**, 147–163.

39 A. Sluiter, B. Hames, R. Ruiz, C. Scarlata, J. Sluiter, D. Templeton and D. Crocker, *Natl. Renew. Energy Lab.*, 2012, 17.

40 W. T. Chen, Y. Zhang, T. H. Lee, Z. Wu, B. Si, C. F. F. Lee, A. Lin and B. K. Sharma, *Nat. Sustain.*, 2018, **1**, 702–710.

41 D. J. R. Cherney, in *Forage evaluation in ruminant nutrition.*, CABI, Wallingford, 2009, pp. 281–300.

42 P. W. Baker, A. Charlton and M. D. C. Hale, *Bioresour. Technol.*, 2015, **189**, 81–86.

43 J. Deng, T. Xiong, H. Wang, A. Zheng and Y. Wang, *ACS Sustain. Chem. Eng.*, 2016, **4**, 3750–3756.

44 H. Zabed, J. N. Sahu, A. N. Boyce and G. Faruq, *Renew. Sustain. Energy Rev.*, 2016, **66**, 751–774.

45 K. Kim, D. G. Lim, C. W. Han, S. Osswald, V. Ortalan, J. P. Youngblood and V. G. Pol, *ACS Sustain. Chem. Eng.*, 2017, **5**, 8720–8728.

46 H. Zhang, W. Zhang, H. Ming, J. Pang, H. Zhang, G. Cao and Y. Yang, *Chem. Eng. J.*, 2018, **341**, 280–288.

47 A. Oya and S. Otani, *Carbon*, 1979, **17**, 131–137.

48 J. Hoekstra, A. M. Beale, F. Soulimani, M. Versluijs-Helder, D. Van De Kleut, J. M. Koelewijn, J. W. Geus and L. W. Jenneskens, *Carbon*, 2016, **107**, 248–260.

49 K. Swennen, C. M. Courtin and J. a Delcour, *Crit. Rev. Food Sci. Nutr.*, 2006, **46**, 459–71.

50 J. Yu, N. Paterson, J. Blamey and M. Millan, *Fuel*, 2017, **191**, 140–149.

51 C. Xia and S. Q. Shi, *Green Chem.*, 2016, **18**, 2063–2071.

52 Y. Li, Z. Teng, P. Chen, Y. Song, Y. Luo and Q. Wang, *J. Colloid Interface Sci.*, 2015, **438C**, 130–137.

53 F. Xie, Z. Xu, A. C. S. Jensen, H. Au, Y. Lu, V. Araullo-Peters, A. J. Drew, Y. Hu and M. Titirici, *Adv. Funct. Mater.*, 2019, **29**, 1901072.

54 C. Peng, X. Yan, R. Wang, J. Lang, Y. Ou and Q. Xue, *Electrochim. Acta*, 2013, **87**, 401–408.

55 P. C. Tsai, S. C. Chung, S. K. Lin and A. Yamada, *J. Mater. Chem. A*, 2015, **3**, 9763–9768.

56 D. Qin, F. Zhang, S. Dong, Y. Zhao, G. Xu and X. Zhang, *RSC Adv.*, 2016, **6**, 106218–106224.

57 Y.-J. Kang, S. C. Jung, J. W. Choi and Y.-K. Han, *Chem. Mater.*, 2015, **27**, 5402–5406.

58 M. Winter, *J. Electrochem. Soc.*, 1998, **145**, 428.

59 E. Irisarri, A. Ponrouch and M. R. Palacin, *J. Electrochem. Soc.*, 2015, **162**, A2476–A2482.

60 J. Wang, X. Yan, Z. Zhang, H. Ying, R. Guo, W. Yang and W. Han, *Adv. Funct. Mater.*, 2019, **1904819**, 1904819.

61 D. A. Stevens and J. R. Dahn, *J. Electrochem. Soc.*, 2000, **147**, 1271.

62 H. Hou, X. Qiu, W. Wei, Y. Zhang and X. Ji, *Adv. Energy Mater.*, 2017, **7**, 1602898.

63 Y. Wen, K. He, Y. Zhu, F. Han, Y. Xu, I. Matsuda, Y. Ishii, J. Cumings and C. Wang,

Nat. Commun., 2014, **5**, 4033.

64 Y. Cao, L. Xiao, M. L. Sushko, W. Wang, B. Schwenzer, J. Xiao, Z. Nie, L. V. Saraf, Z. Yang and J. Liu, *Nano Lett.*, 2012, **12**, 3783–3787.

65 J. Hao, Y. Wang, C. Chi, J. Wang, Q. Guo, Y. Yang, Y. Li, X. Liu and J. Zhao, *Sustain. Energy Fuels*, 2018, **2**, 2358–2365.

66 C. Bommier, T. W. Surta, M. Dolgos and X. Ji, *Nano Lett.*, 2015, **15**, 5888–5892.

67 Y. P. Gao, Z. B. Zhai, K. J. Huang and Y. Y. Zhang, *New J. Chem.*, 2017, **41**, 11456–11470.

68 A. Gomez-Martin, J. Martinez-Fernandez, M. Ruttert, A. Heckmann, M. Winter, T. Placke and J. Ramirez-Rico, *ChemSusChem*, 2018, **11**, 2776–2787.

69 X. Chen, L. P. Lv, W. Sun, Y. Hu, X. Tao and Y. Wang, *J. Mater. Chem. A*, 2018, **6**, 13705–13716.

70 B. Hou, Y. Wang, Q. Ning, W. Li, X. Xi, X. Yang, H. Liang, X. Feng and X. Wu, *Adv. Mater.*, 2019, **31**, 1903125.

71 C. Bommier, X. Ji and P. A. Greaney, *Chem. Mater.*, 2019, **31**, 658–677.

72 M. Wahid, Y. Gawli, D. Puthusseri, A. Kumar, M. V. Shelke and S. Ogale, *ACS Omega*, 2017, **2**, 3601–3609.

73 E. M. Lotfabad, J. Ding, K. Cui, A. Kohandehghan, W. P. Kalisvaart, M. Hazelton and D. Mitlin, *ACS Nano*, 2014, **8**, 7115–7129.

74 L. Tao, Y. Huang, Y. Zheng, X. Yang, C. Liu, M. Di, S. Larpkiattaworn, M. R. Nimlos and Z. Zheng, *J. Taiwan Inst. Chem. Eng.*, 2018, **0**, 1–10.

75 J. Wang, L. Yan, Q. Ren, L. Fan, F. Zhang and Z. Shi, *Electrochim. Acta*, 2018, **291**, 188–196.

76 J. Zhang, Z. Zhang and X. Zhao, *RSC Adv.*, 2015, **5**, 104822–104828.

77 T. C. Nirmale, B. B. Kale and A. J. Varma, *Int. J. Biol. Macromol.*, 2017, **103**, 1032–1043.